

## Diffusion of noiseless active particles in a planar convection array

Qingqing Yin<sup>1</sup>, Jianli Liu<sup>1</sup>, Yunyun Li<sup>1,\*</sup> and Fabio Marchesoni<sup>1,2,†</sup>

<sup>1</sup>MOE Key Laboratory of Advanced Micro-Structured Materials and Shanghai Key Laboratory of Special Artificial Microstructure Materials and Technology, School of Physics Science and Engineering, Tongji University, Shanghai 200092, China

<sup>2</sup>Dipartimento di Fisica, Università di Camerino, I-62032 Camerino, Italy



(Received 31 January 2024; accepted 15 May 2024; published 17 June 2024)

We investigated, both analytically and numerically, the dynamics of a noiseless overdamped active particle in a square lattice of planar counter-rotating convection rolls. Below a first threshold of the self-propulsion speed, a fraction of the simulated particle's trajectories spatially diffuse around the convection rolls, whereas the remaining trajectories remain trapped inside the injection roll. We detected two chaotic diffusion regimes: (i) below a second, higher threshold of the self-propulsion speed, the particle performs a random motion characterized by asymptotic normal diffusion. Long superdiffusive transients were observed for vanishing small self-propulsion speeds. (ii) above that threshold, the particle follows chaotic running trajectories with speed and orientation close to those of the self-propulsion vector at injection and its dynamics is superdiffusive. Chaotic diffusion disappears in the ballistic limit of extremely large self-propulsion speeds.

DOI: [10.1103/PhysRevE.109.064211](https://doi.org/10.1103/PhysRevE.109.064211)

### I. INTRODUCTION

In this paper we revisit the recurrent problem of the overdamped dynamics of a massless particle diffusing in a square lattice of planar counter-rotating convection rolls [1,2]. The reference model is represented by a disk of coordinates  $x$  and  $y$ , suspended in a two-dimensional (2D) stationary laminar flow with periodic center-symmetric stream function [1,2]

$$\psi(x, y) = (U_0 L / 2\pi) \sin(2\pi x / L) \sin(2\pi y / L), \quad (1)$$

where  $U_0$  is the maximum advection speed and  $L$  the size of the flow unit cell, which consists of four counter-rotating flow subcells, also termed convection rolls (see Fig. 1). The case of a tracer suspended in a chaotic flow would require a more sophisticated hydrodynamic modeling [3], which rests outside the purpose of the present investigation.

The disk's dynamics can be formulated by means of two coupled nonlinear equations:

$$\begin{aligned} \dot{\mathbf{r}} &= \mathbf{v}_\psi + \mathbf{v}_0, \\ \dot{\boldsymbol{\theta}} &= (\alpha/2) \nabla \times \mathbf{v}_\psi, \end{aligned} \quad (2)$$

where  $\mathbf{v}_\psi = \mathbf{J} \cdot \nabla \psi$ , with  $\mathbf{J}$  denoting the symplectic unit matrix  $\begin{pmatrix} 0 & 1 \\ -1 & 0 \end{pmatrix}$ , is the advection velocity, and  $\mathbf{v}_0 = v_0(\cos \theta, \sin \theta)$  is a tunable drag due either to an external force (with  $\alpha = 0$ ) in the case of a passive disk, or to some self-propulsion mechanism in the case of an active disk (with  $\alpha = 1$ , when adopting Faxén's second law [4,5]).

Particle dynamics of Eqs. (1) and (2) has been studied under diverse physical conditions and a rich phenomenology has emerged. The reference model [1] represents the unbiased dynamics of a passive disk with  $\mathbf{v}_0 = 0$ . In the absence of inertial

effects, a suspended tracer follows necessarily a streamline of the Eulerian velocity field  $\mathbf{v}_\psi(x, y)$ . The incompressible nature of the advection field  $\nabla \cdot \mathbf{v}_\psi = 0$  implies that a suspension of noninteracting disks, if initially uniform, must remain uniform at any time.

By a closer inspection, one concludes that the symplectic form of Eq. (2) holds also in the presence of an external drag  $\mathbf{v}_0$ , not explicitly dependent on the particle's position  $\mathbf{r}$ . Let us consider first the case of  $\alpha = 0$ , that is a fixed external drag oriented at an angle  $\theta$ , with respect to the horizontal  $x$  axis. As noted first in Ref. [6] for  $\theta = -\pi/2$ , and later detailed in Ref. [7] for any  $\theta$ , the external forcing term changes completely the dynamics of a uniform particle suspension. Despite the apparent spatial uniformity, individual disks can be either trapped inside a subcell, where they retrace closed orbits around an off-center stability point defined by the condition  $\mathbf{v}_\psi + \mathbf{v}_0 = 0$ , or cross the advection cells when running along the flow-boundary layers bordering each subcell. These grow wider with increasing  $v_0$  until for  $v_0 > U_0/\sqrt{2}$  the trapping (or "retention") regions disappear at all.

Adding an inertial term to the first Eq. (2) (not shown) impacts the dynamics of the particle suspension in two ways [7]: (i) the retention regions dissolve over time, that is trajectory trapping can only be detected as a transient effect; (ii) an initially uniform particle distribution shrinks along the stationary flow streams of the running massive particles. More sophisticated modeling of the inertial effects may lead to chaotic trajectories [8] or exotic particle responses, like an absolute negative mobility [9].

Another variation of Eq. (2) consists in replacing the constant drag  $\mathbf{v}_0$  with the fluctuating term  $\boldsymbol{\xi}(t) = (\xi_x(t), \xi_y(t))$ , where  $\xi_i(t)$  with  $i = x, y$  are stationary, independent, delta-correlated Gaussian noises  $\langle \xi_i(t) \xi_j(0) \rangle = 2D_0 \delta_{ij} \delta(t)$  [10–13]. The first Eq. (2) thus turns into a Langevin equation: Not only the uniformity of the initial suspension distribution is

\*Contact author: yunyunli@tongji.edu.cn

†Contact author: fabio.marchesoni@pg.infn.it

preserved, but a single diffusing tracer subject to periodic boundary conditions would cover the advection unit cell uniformly, which defines the diffusive process as ergodic. On increasing  $D_0$ , its asymptotic diffusion constant  $D$  changes from  $D = \kappa \sqrt{D_L D_0}$ , for  $D_0 < D_L$  (advective diffusion), to  $D = D_0$ , for  $D_0 > D_L$  (free diffusion). For the convection array of Eq. (1),  $\kappa \simeq 1.07$  [10]. The crossover between these two diffusion regimes occurs at  $D_0 \simeq D_L$  and appears to be quite sharp [14]. The quantity  $D_L = U_0 L / 2\pi$  can be regarded as the natural diffusion scale of the advection field. This property was explained [10–13] by noticing that for  $D < D_L$  spatial diffusion across the subcell separatrices is restricted to the boundary-flow layers delimiting the individual advection rolls.

The symplectic form of the first Eq. (2) holds even if the vector  $\mathbf{v}_0$  evolves in time indirectly depending on the particle's position. An example was addressed by the authors of Ref. [15], who investigated the advection of an active particle [16–19] with constant speed  $v_0$  and angle  $\theta$  turning subject to the advection torque of the second Eq. (2) with  $\alpha = 1$ . They concluded that such a self-propelling tracer would either move along quasiperiodic orbits confined to a delimited region at the center of the convection rolls, or follow unbounded chaotic trajectories straddling the roll separatrices, if set off in a flow-boundary layer. These two distinct regions would be separated by an invariant surface, acting as a sort of effective “transport barrier,” which they predicted to vanish for  $v_0 \gtrsim (2\pi/3)U_0$ , i.e., at values of  $v_0$  larger than predicted for a passive dragged-advected particle [7].

More recently [14], the diffusion model of Ref. [15] has been generalized by replacing  $\mathbf{v}_0$  with  $v_0(\cos\theta, \sin\theta) + \xi(t)$  in the first Eq. (2) and possibly adding a rotational noise in the r.h.s. of the second Eq. (2). It is the puzzling dependence of the resulting particle's diffusion constant  $D$  on  $v_0$  and  $D_0$  that led us to revisit the original noiseless model of Ref. [15], thus discovering a richer phenomenology than previously reported. In particular, extensive numerical simulations revealed that below a first  $v_0$  threshold, much lower than predicted in Ref. [15], a fraction of the injected particle's trajectories spatially diffuse across the convection rolls, whereas the remaining trajectories remain trapped inside the injection roll. Two diffusion regimes of chaotic nature are identified: Below a second, higher  $v_0$  threshold, the particle performs a random motion characterized by asymptotic normal diffusion; above that threshold, the particle executes a superdiffusive dynamics, its chaotic running trajectories assuming speed and orientation close to those of the self-propulsion vector at injection.

The contents of this paper is organized as follows. In Sec. II we separate trapped from running trajectories, analyze area and geometry of the starting trapping regions, and determine the value of the first threshold of the self-propulsion speed, above which trapping is suppressed. To keep our analysis as simple as possible, we only considered small-size circular disks. Special geometries are known to strongly affect advective diffusion (like in the case of needles [15] or elastic fibers [20,21]). In Sec. III we characterize the chaotic nature of the running trajectories: ergodic and isotropically diffusive for self-propulsion speeds below the second, higher threshold, and quasiballistic above it, with orientation and average

speed conditioned by the initial value of the self-propulsion vector. Below the first threshold, the coexistence of trapped and running trajectories is marked by long superdiffusive transients. In Sec. IV we focus on the disk's chaotic diffusion under different dynamical regimes. Between the first and second threshold the particle undergoes normal diffusion, independently of the initial conditions. Above the second threshold, the chaotic nature of the quasiballistic trajectories gives rise to unexpected superdiffusive manifestations, which vanish only for exceeding large values of the self-propulsion speed.

## II. TRAPPED TRAJECTORIES

For reader's convenience, we now rewrite explicitly the model equations (2) with  $\alpha = 1$ :

$$\begin{aligned}\dot{x} &= U_0 \sin(2\pi x/L) \cos(2\pi y/L) + v_0 \cos\theta, \\ \dot{y} &= -U_0 \cos(2\pi x/L) \sin(2\pi y/L) + v_0 \sin\theta, \\ \dot{\theta} &= \Omega_L \sin(2\pi x/L) \sin(2\pi y/L),\end{aligned}\quad (3)$$

where  $\Omega_L = 2\pi U_0/L$  is a characteristic advection angular frequency. These ordinary differential equations were numerically integrated by means of a standard Mil'shtein scheme [22] to allow adding fluctuating terms as appropriate for a comparison. Particular caution was exerted when computing asymptotic quantities, like the effective running speed

$$\mathbf{V}_{\text{eff}} = \lim_{t \rightarrow \infty} \mathbf{r}(t)/t, \quad (4)$$

to properly account for the chaotic nature of the advected disk's trajectories. In our code, we used the advection field parameters  $U_0$  and  $L$  to set convenient length and time units, respectively,  $L$  and  $\Omega_L^{-1}$ . In the simulation results reported below, we set  $L = 2\pi$  and  $U_0 = 1$ , so that the time unit is 1. Therefore, tunable parameters in our analysis are the self-propulsion speed  $v_0$ , and the initial conditions  $x(0)$ ,  $y(0)$ , and  $\theta(0)$ .

To explore the chaotic dynamics of an advected active disk, we integrated the trajectories corresponding to a uniform distribution of  $N = 10^4$  starting positions,  $(x(0), y(0))$ , in the bottom-left counterclockwise rotating roll of Fig. 1, for different self-propulsion speeds  $v_0$ , and initial orientations  $\theta(0)$ . We ran our integration code for a long time,  $t = 10^5$  or even longer as appropriate, and thus distinguished between trapped and running trajectories. In Fig. 2 we marked with red (blue) dots the starting positions of the trapped (running) trajectories. In consideration of the incompressibility of the configuration space  $(x, y)$ , this procedure defines a consistent measure of the areas of starting trapping (red) and running (blue) regions. One notices immediately that the starting trapping regions (i) shrink with increasing  $v_0$  [Figs. 2(a)–2(c)]; (ii) are localized on the subcell side where advection and self-propulsion point in opposite directions [Figs. 2(c) and 2(d)]. Noticing that the starting trapping region shifts along the roll boundary as  $\theta(0)$  is increased, one is not surprised to observe that a trapped disk traces over time bound and generally not closed trajectories that encircle the roll center [Figs. 3(a)–3(c)]. The trapping regions of Fig. 2 resemble the retention regions of Refs. [6,7] with an important difference (see the Appendix for more details). There,  $\theta = \theta(0)$  at any time, because there is

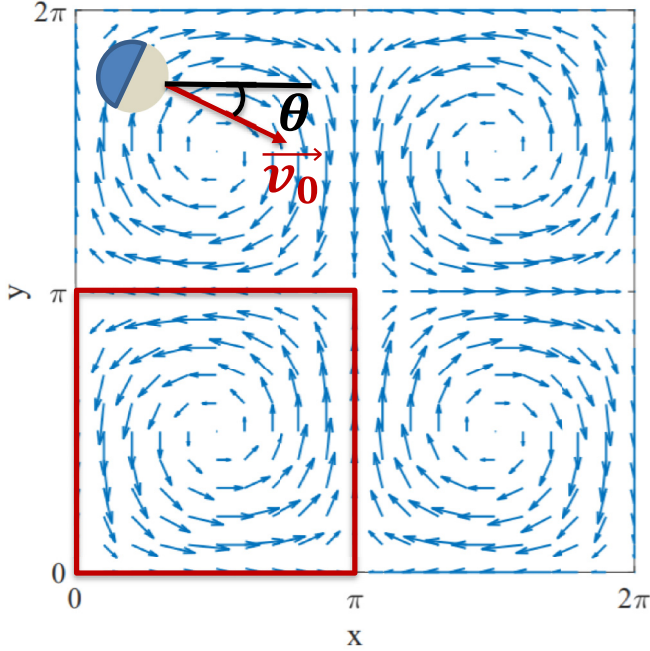


FIG. 1. Advected active particle in the 2D periodic convection array of Eq. (1) with  $L = 2\pi$ . The unit cell of  $\psi(x, y)$  consists of four counter-rotating rolls. If not stated otherwise, the trajectories reported in this paper are referred to the bottom-left counterclockwise rotating roll marked in red.

no advection stream exerting a torque on the disk ( $\alpha = 0$ ). Accordingly, the disk retraces closed orbits inside a time-invariant retention region (see, e.g., Figs. 2 and 3 of Ref. [7]). Here, instead, the angle  $\theta(t)$  is periodically modulated as the disk trajectory winds up around the advection center. As a result, points of the starting trapping region get dispersed over time and eventually distributed along a uniform ringlike structure encircling the roll center [Fig. 2(f)]. Of course, their number,  $N_t$ , is conserved as to be expected for the symplectic dynamics of Eq. (3) [15]. More importantly, over time, due to the advection torque, the starting red points mix together with the blue ones, while conserving their number  $N_t$ . Contrary to Ref. [15], no definite “barrier” separates trapped from running trajectories.

Another difference between the trajectories with ( $\alpha = 1$ ) and without ( $\alpha = 0$ ) advection torque is that for  $\alpha = 0$  the area of the time-independent retention region, i.e.,  $N_t$ , depends on the choice of  $\theta(0)$ , whereas for  $\alpha = 1$  the area of the starting trapping region is apparently independent of  $\theta(0)$  [Fig. 3(d)]. Moreover, contrary to Fig. 4 of Ref. [7], the curves of  $N_t$  versus  $v_0$  are the same for both a fixed  $\theta(0) = 0$ , and a uniform distribution of the initial orientation of the self-propulsion vector  $\mathbf{v}_0$ , at the starting positions. In the latter case, the spatial distribution of the starting points of the trapped trajectories is indistinguishable from that obtained from the time evolution of any starting trapping region [Fig. 2(f)]. Stated otherwise, the measure of the trapping region does not change owing to the combined effect of the different circulation times [23] and the vanishing time averages of  $\dot{\theta}(t)$  along the winding trajectories (no matter what the integration time).

A further difference between the invariant trapping regions with  $\alpha = 0$  [7] and the starting trapping regions reported here, is the appearance of symmetrically distributed islets of starting trapping points, bordering the main trapping region [Figs. 2(b)–2(d)]. We verified that such islets are dense and stable [compare Figs. 2(c) and 2(e)], also for much longer integration runs. Trajectories originating in the trapping islets appear to be more chaotic than those originating at the center of the main trapping region [compare Figs. 3(a) and 3(c)].

As anticipated when first presenting Fig. 2, the starting trapping region shrinks with increasing  $v_0$ . This effect is quantified by the decay of the curves  $N_t$  versus  $v_0$  plotted in Fig. 3(d). From a detailed trajectory analysis we set the  $v_0$  threshold for the disappearance of the starting trapping region at  $v_{\text{th}}^{(1)} \simeq 0.42U_0$ . Our numerical estimate of  $v_{\text{th}}^{(1)}$  is quite lower than reported in Ref. [15], but more consistent with the analytical result obtained in Ref. [7] for  $\alpha = 0$  and constant  $\theta$ , that is,  $v_{\text{th}}^{(1)} = U_0/(|\cos\theta| + |\sin\theta|)$ , whence, on varying  $\theta$  with  $\alpha = 0$ , one expects  $\sqrt{2}/2 \leq v_{\text{th}}^{(1)} \leq 1$ .

### III. RUNNING TRAJECTORIES

The running trajectories exhibit qualitatively distinct behaviors depending on the value of the self-propulsion speed. By inspecting Figs. 2(a)–2(c) one notices that at very low  $v_0$ , when the starting trapping region extends over the center of the convection roll, the time evolution of the blue starting points is confined to rather narrow layers bordering the  $\psi(x, y)$  subcells. Accordingly, the corresponding running trajectories tend to follow the cell separatrices, often encircling a single roll, while maintaining a persistent overall direction. The advected disk thus appears to diffuse isotropically by executing long jumps either parallel or orthogonal to the  $x$  axis [Fig. 4(a)]. Since close to the separatrices the advection torque is suppressed [see third Eq. (3)], the angle  $\theta(t)$  varies very little around its initial value,  $\theta(0)$ , over the entire integration run [Fig. 4(d)]. We remind that  $\theta(t)$  should not be mistaken for the trajectory orientation in the plane  $x$ - $y$ . With increasing  $v_0$ , the running trajectories penetrate the convection rolls, mixing with the coexisting trapped trajectories, if any. The trajectories appear to diffuse isotropically, resembling those of a Brownian particle [Fig. 4(b)], with the orientation of the self-propulsion vector  $\mathbf{v}_0$  strongly randomized by the advection torque [Fig. 4(e)]. In stark contrast with the previous dynamical regime, here  $\mathbf{v}_0$  appears to closely line up with the Eulerian velocity vector  $\mathbf{v}_\psi$ . Consequently, as the trajectory encircles either a clock- or counterclockwise convection roll, the self-propulsion angle  $\theta$  varies by an amount of the order of  $\mp\pi$  with time constant of the order of  $2\pi/\Omega_L$ . Thus, as discussed in Sec. IV, the resulting random variable  $\theta(t)$  appears to undergo normal diffusion [inset of Fig. 4(e)].

These diffusive scenarios give way to a quasiballistic dynamics for self-propulsion speeds above a second, quite high threshold,  $v_{\text{th}}^{(2)}$ . As shown in Fig. 4(c), the running trajectories cut now across the  $\psi(x, y)$  cells with average drift vector, Eq. (4), depending on the combined effects of self-propulsion and advection. The orientation  $\theta_{\text{eff}}$  of such trajectories is attracted either parallel to the closest diagonal through the stagnation regions at the corners of the

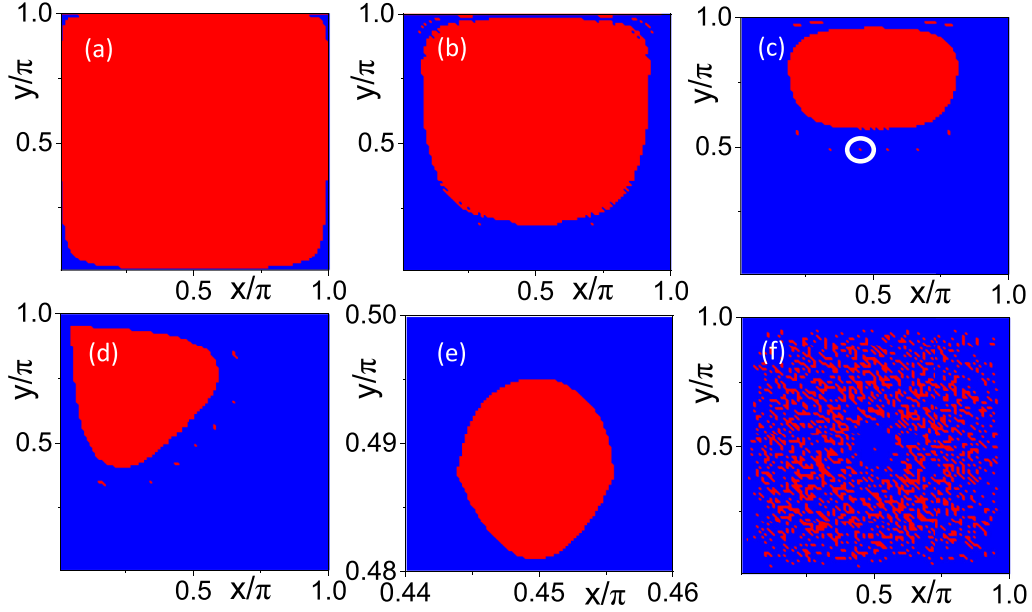


FIG. 2. Trapping areas in the counterclockwise rotating roll marked in red in Fig. 1.  $N = 10^4$  particles were injected in that subcell with uniform spatial distribution, but fixed orientation,  $\theta(0)$ : 0 in (a)–(c) and (e);  $\pi/4$  in (d); uniformly distributed in the range  $[0, 2\pi]$  in (f), and different self-propulsion speed  $v_0 = 0.01$  in (a), 0.1 in (b), and 0.2 in (c)–(f). Numerical integrations ran up to  $t = 10^5$ : red (blue) dots mark the starting point of a trapped (running) trajectory. The plot in (e) is a blow up of the isolated red islet encircled in white in (c), while in (f) are the starting red and blue points of (c) at  $t = 10^5$ . The advection parameters are  $L = 2\pi$  and  $U_0 = 1$ .

$\psi(x, y)$  subcells,  $\theta_{\text{eff}} \simeq \pi/4$ , or its initial value,  $\theta_{\text{eff}} = \theta(0)$ , depending on the initial conditions [Figs. 4(f) and 5].

Above the threshold  $v_{\text{th}}^{(2)}$  [Fig. 6(a)], the modulus  $V_{\text{eff}}$  of the drift vector of Eq. (4), jumps abruptly from nearly zero up to close but not equal to  $v_0$  [Fig. 6(b)]. It shows a minimum when  $\mathbf{v}_0$  is initially oriented diagonally across the advection field. The magnitude of the  $V_{\text{eff}}$  dip weakly depends on the

starting position  $(x(0), y(0))$ , and vanishes with increasing  $v_0$ . Accordingly, the threshold  $v_{\text{th}}^{(2)}$  is quite sensitive to both the initial position and orientation of the advected particle. In any case,  $v_{\text{th}}^{(2)}$  is much larger than  $U_0$  and, therefore,  $v_{\text{th}}^{(1)}$ . In conclusion, the quasiballistic regime is characterized by chaotic trajectories, whose angular spreading appears amplified in correspondence with large  $\theta_{\text{eff}} - \theta(0)$  differences [Fig. 5(d)–5(e)].

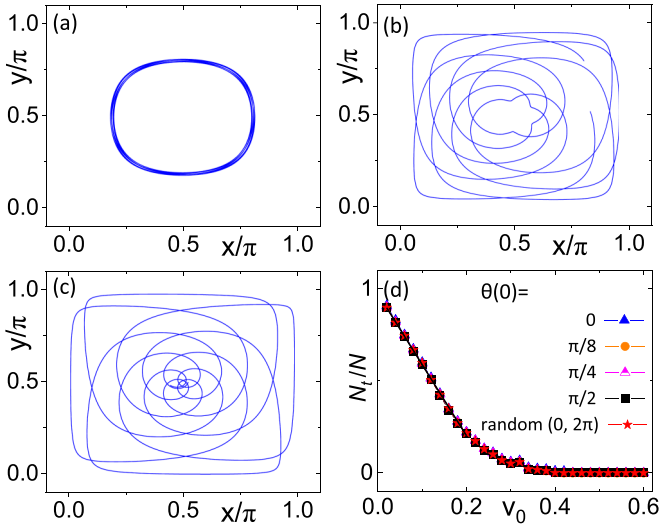


FIG. 3. Trapped trajectories in the counterclockwise rotating roll marked in red in Fig. 1 for  $v_0 = 0.2$ ,  $\theta(0) = 0$ , and different starting positions  $(x(0), y(0))$ : (a)  $(0.5, 0.8)\pi$ , (b)  $(0.8, 0.8)\pi$ , and (c)  $(0.4475, 0.4925)\pi$ , i.e., close to the center, the border, and inside the encircled islet of the trapping region of Fig. 2(c). The fraction of trapped trajectories,  $N_t/N$  vs  $v_0$ , is plotted in (d) for different  $\theta(0)$  (see legend). The advection parameters are  $L = 2\pi$  and  $U_0 = 1$ .

#### IV. CHAOTIC DIFFUSIVITY

We characterize now the running trajectories by looking at their diffusive properties. To this purpose we computed the mean-square displacements (MSD) of the spatial coordinate  $x$  and the self-propulsion angle  $\theta$ . The averages were computed either over time,

$$\begin{aligned} \Delta x^2(t) &= \lim_{\tau \rightarrow \infty} [\langle x^2(t + \tau) \rangle - \langle x(\tau) \rangle^2], \\ \Delta \theta^2(t) &= \lim_{\tau \rightarrow \infty} [\langle \theta^2(t + \tau) \rangle - \langle \theta(\tau) \rangle^2], \end{aligned} \quad (5)$$

or over the initial conditions,

$$\begin{aligned} \Delta x^2(t) &= \langle x^2(t) \rangle - \langle x(0) \rangle^2, \\ \Delta \theta^2(t) &= \langle \theta^2(t) \rangle - \langle \theta(0) \rangle^2. \end{aligned} \quad (6)$$

In the following, we only display MSD's [Eq. (6)] averaged over a uniform distribution of  $\theta(0)$ .

The running trajectories for  $v_0 < v_{\text{th}}^{(2)}$  exhibit diffusive properties independent of the initial conditions, with vanishing asymptotic averages  $\langle [x(t) - x(0)] \rangle$  and  $\langle [\theta(t) - \theta(0)] \rangle$  (not shown). As a consequence, for large  $t$  the MSD's of Eqs. (5) and (6) coincide [compare, e.g.,  $\Delta \theta^2(t)$  in Figs. 4(e) and 7(a)], thus corroborating the ergodicity

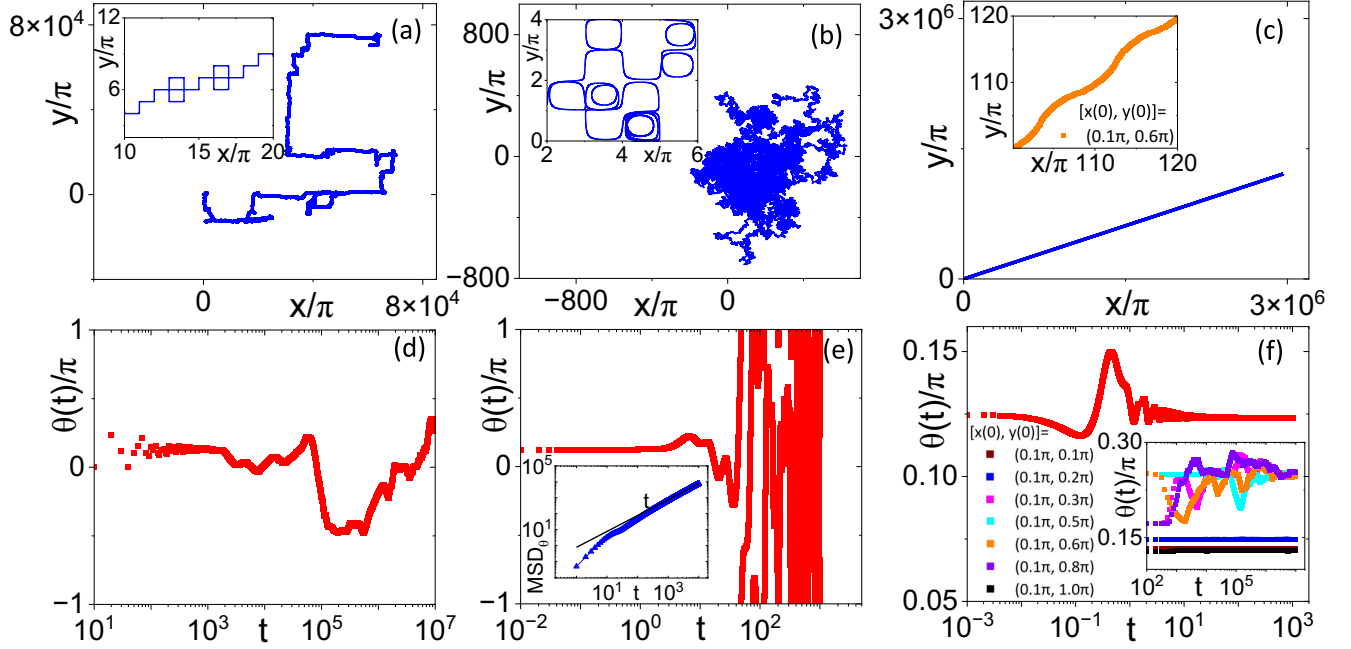


FIG. 4. Running trajectories for (a)  $v_0 = 0.001$ , (b)  $v_0 = 0.1$ , (c)  $v_0 = 10$ , with initial conditions  $(x(0), y(0)) = (0.001, 0.001)\pi$  and  $\theta(0) = \pi/8$ , and integration time  $t = 10^7$  (shorter-time details are shown in the insets). The corresponding angular observable  $\theta(t) \pmod{\pi}$  is plotted in the panels of the lower row for (d)  $v_0 = 0.001$ , (e)  $v_0 = 0.1$ , and (f)  $v_0 = 10$ . In the insets of (c) and (f) additional data are reported for different initial starting positions (see legends). In the inset of (e),  $\Delta\theta(t)$ , Eqs. (5) is plotted vs  $t$ ; the linear slope was drawn to guide the eye. The advection parameters are  $L = 2\pi$  and  $U_0 = 1$ .

claim of Sec. II. Moreover, both MSD functions approach an oblique asymptote, which is a signature of normal diffusion [Figs. 7(a) and 7(b)]. In contrast with the Brownian dynamics [24], here normal diffusion must be ascribed to the chaotic dynamics of the advected particle. [In the present model one speaks of Lagrangian chaos since the Eulerian velocities on the r.h.s. of Eq. (2) are non-chaotic.] Due to the orientational

randomness of the vector  $\mathbf{v}_0(t)$ , a slowly self-propelling disk diffuses isotropically; self-propulsion only helps it cross the roll separatrices, while advection is responsible for the spatial and angular displacements. Based on this argument, one estimates the relevant diffusion constants [24],  $D = \lim_{t \rightarrow \infty} \Delta x^2(t)/2t \simeq (1 - N_i/N)(L/2)^2/[2(2\pi/\Omega_L)]$  and  $D_\theta = \lim_{t \rightarrow \infty} \Delta \theta^2(t)/2t \simeq (1 - N_i/N)(\pi)^2/[2(2\pi/\Omega_L)]$ .

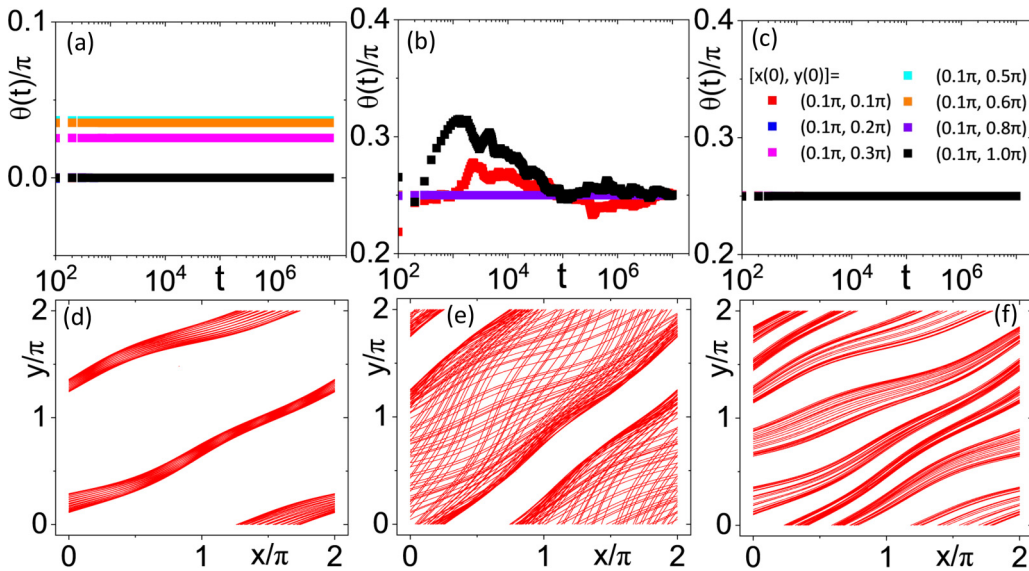


FIG. 5. Running trajectories: orientation of  $\mathbf{v}_0(t)$  for  $\theta(0) = 0$  (a),  $\pi/6$  (b), and  $\pi/4$  (c),  $v_0 = 10$ , and different starting positions [see legend in (c)]. The asymptotic value  $\theta(t)$  defines the orientation  $\theta_{\text{eff}}$  of the vector  $\mathbf{V}_{\text{eff}}$  of Eq. (4). Trajectory samples of length  $t = 100$ , folded in the bottom-left subcell of the  $\psi(x, y)$  unit of Fig. 1 are displayed for  $v_0 = 10$ ,  $\theta(0) = \pi/8$  [see Figs. 4(c) and 4(f)], and  $(x(0), y(0)) = (0.1, 0.2)\pi$  (d),  $(0.1, 0.5)\pi$  (e), and  $(0.1, 0.8)\pi$  (f). The advection parameters are  $L = 2\pi$  and  $U_0 = 1$ .

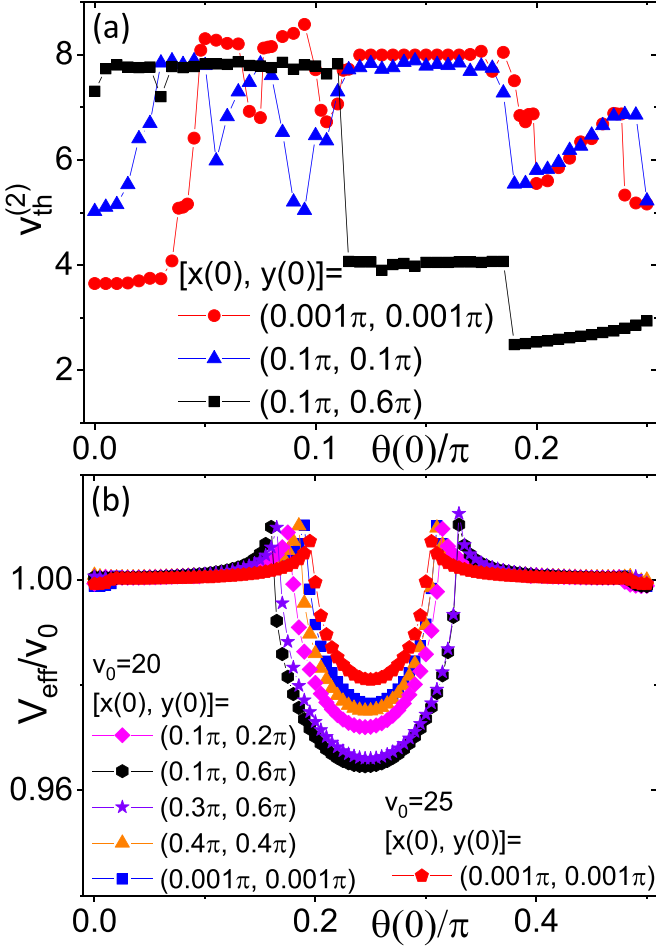


FIG. 6. Running trajectories: (a)  $v_{\text{th}}^{(2)}$  vs  $\theta(0)$  for different starting positions (see legend); (b)  $V_{\text{eff}}$  vs  $\theta(0)$  for different  $v_0$  and starting positions (see legend). In both the advection parameters are  $L = 2\pi$  and  $U_0 = 1$  and the integration run length is  $t = 10^7$ .

For the  $\psi(x, y)$  parameters  $U_0 = 1$  and  $L = 2\pi$  adopted throughout this paper,  $D = D_\theta \simeq (1 - N_t/N)\pi/4$ , consistently with our numerical data. A similar behavior is reported in Ref. [8] for a driven-advected particle in an inertial 2D convection array with  $\alpha = 0$ .

For exceedingly small  $v_0$  values,  $v_0 \ll v_{\text{th}}^{(1)}$ , in Fig. 4(a) the running trajectories were shown to jump multiple rolls parallel to the  $x$  or  $y$  axis before changing direction. Accordingly, the corresponding spatial MSD's develop a prominent superdiffusive transient, which grows quadratically with  $t$  [Fig. 7(b)]. A similar behavior was reported in Ref. [25], whereby the convection-square array and the low self-propulsion speed are replaced by a square lattice potential and a strong inertial term.

In the quasiballistic regime  $v_0 > v_{\text{th}}^{(2)}$ , the trajectories appear to depend on the initial conditions (Figs. 4–6), with  $\theta_{\text{eff}} \rightarrow \theta(0)$  and  $V_{\text{eff}} \rightarrow v_0$  in the ballistic limit  $v_0/U_0 \rightarrow \infty$ . For this reason and contrary to Ref. [8], here we restrict our discussion to the time-averaged spatial MSD's of Eqs. (5). For relatively large  $v_0$ , the spatial MSD is largely suppressed regardless of the initial conditions [Fig. 7(c) and 7(d)], as expected when approaching the ballistic limit [24]. More

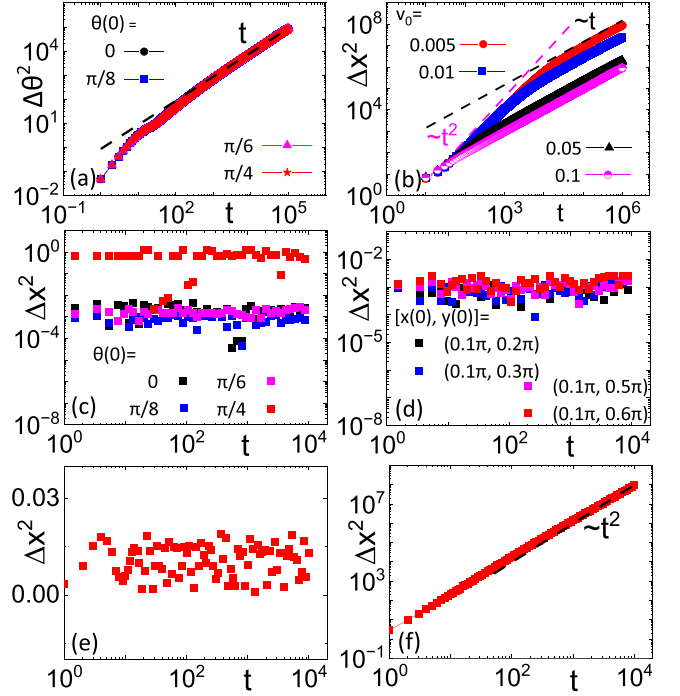


FIG. 7. Chaotic diffusivity: (a)  $\Delta\theta^2(t)$ , Eq. (6),  $v_0 = 0.1$  and different  $\theta(0)$ ; (b)  $\Delta x^2(t)$ , Eq. (5), for a uniform distribution of  $\theta(0)$  and  $v_0 < v_{\text{th}}^{(2)}$  (see legends). In both the starting position is  $(x(0), y(0)) = (0.001, 0.001)\pi$ . The lines  $t$  and  $t^2$  represent the asymptotic and transient-diffusion laws.  $\Delta x^2(t)$ , Eq. (5), has been computed also for  $v_0 = 20$  and (c)  $(x(0), y(0)) = (0.001, 0.001)\pi$  and different  $\theta(0)$ ; (d)  $\theta(0) = \pi/8$  and different starting positions (see legends). In (e) and (f) are the curves  $\Delta x^2(t)$ , Eq. (5), corresponding to the running trajectories of Figs. 5(d) and 5(e), respectively.

interesting is the case of intermediate suprathreshold values of  $v_0$ , where the MSD can be either vanishingly small or grow quadratically with time, depending on the particle starting position. Two examples of different diffusivity are illustrated in Figs. 7(e) and 7(f) for the choice of  $x(0), y(0)$ , and  $\theta(0)$  of Figs. 5(d) and 5(e), respectively. The superdiffusive behavior of Fig. 7(f) appears to be related with the larger chaoticity of the trajectories in Fig. 5(e). A simple argument in support for this result is as follows. Modeling the chaoticity of a running trajectory as a superposition of drifts, with random speeds  $(V_{\text{eff}})_x$ , yields

$$\Delta x^2(t) \simeq [ \langle (V_{\text{eff}})_x^2 \rangle - \langle (V_{\text{eff}})_x \rangle^2 ] t^2, \quad (7)$$

where  $\langle \dots \rangle$  denotes the average taken with respect to the  $(V_{\text{eff}})_x$  distribution. The variance of such distribution may depend on the initial conditions, but vanishes for asymptotically large  $v_0$ .

## V. CONCLUSIONS

In this paper we analyzed in detail the dynamics of an overdamped noiseless self-propelled 2D particle suspended in a square laminar convection array. We separated two types of trajectories, trapped and running, the former disappearing for self-propulsion speeds  $v_0$ , above a first threshold  $v_{\text{th}}^{(1)}$ .

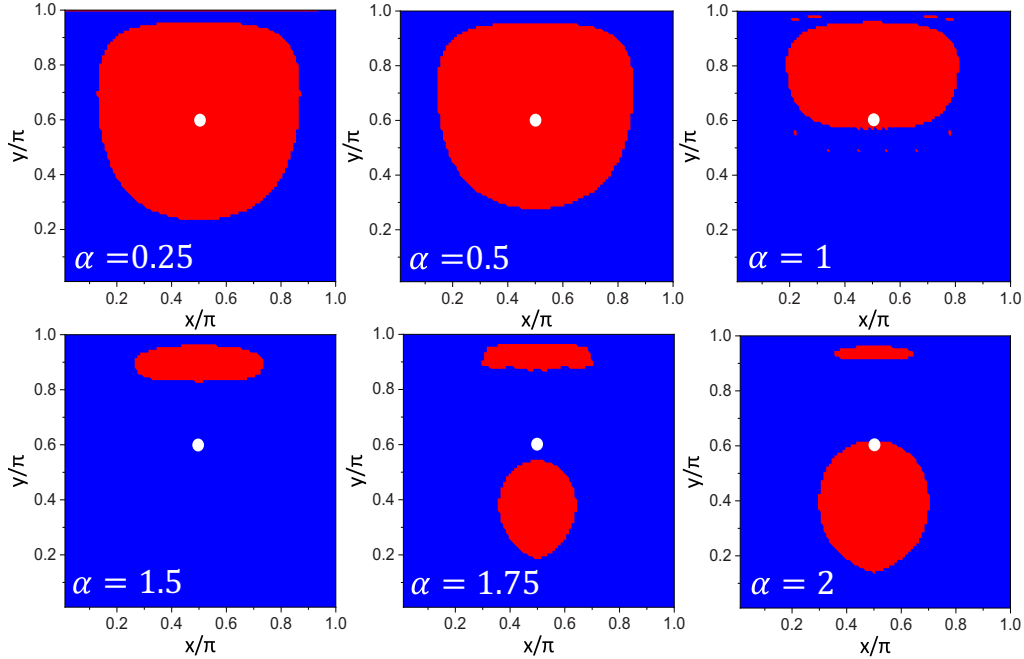


FIG. 8. Trapping regions for  $\theta(0) = 0$ ,  $v_0 = 0.2$  and increasing values of the advection torque strength  $\alpha$  (see legends). All other parameter values are as in Fig. 2.

Contrary to earlier estimates [15], such a threshold turns out to be smaller than the advection speed  $U_0$ . Furthermore we distinguished the running trajectories in diffusive and quasiballistic, for  $v_0$ , respectively, below and above a second threshold  $v_{th}^{(2)}$ , larger than  $U_0$ . Their chaotic nature manifests itself in peculiar properties of the particle spatial diffusivity, ergodic and normal for  $v_0 < v_{th}^{(2)}$ , superdiffusive and

dependent on the initial conditions for  $v_0 > v_{th}^{(2)}$ . Superdiffusive transients are detectable also for  $v_0 \ll v_{th}^{(1)}$ , while diffusion is totally suppressed in the ballistic limit,  $v_0/U_0 \rightarrow \infty$ .

The contribution of Lagrangian chaos to the spatial diffusivity of an advected particle was reported by other authors [8,26] in special cases of massive dragged-advected particles, where inertia was responsible for the onset of chaos.

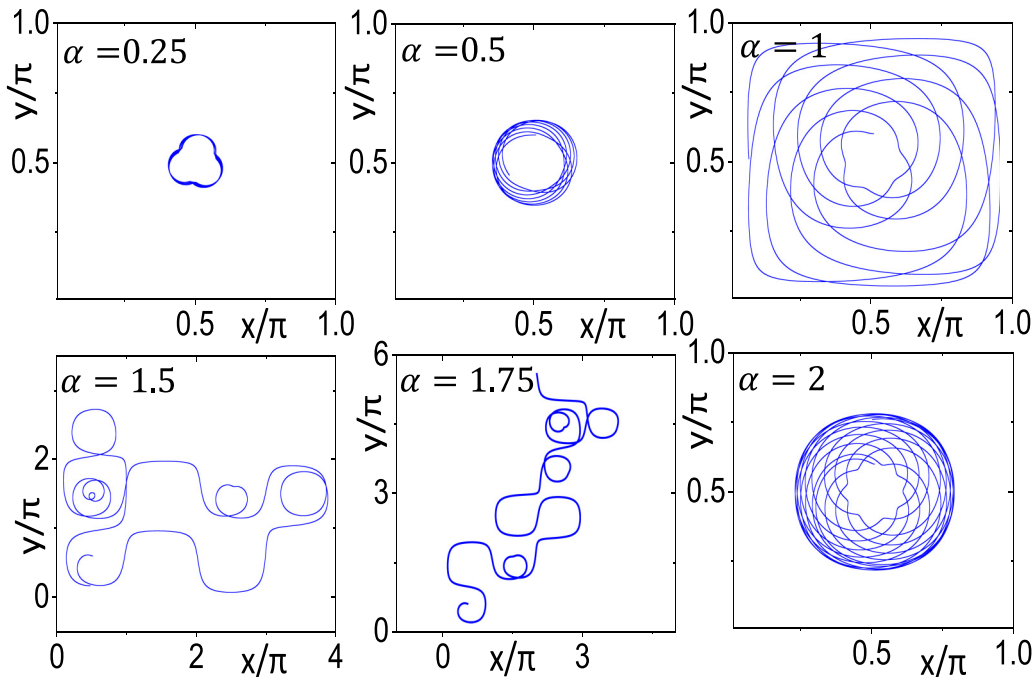


FIG. 9. Trajectories of length  $t = 10^2$  traced by a particle injected at the white dots of the corresponding panels of Fig. 8,  $(x(0), y(0)) = (0.5, 0.6)\pi$ , with  $\theta(0) = 0$ . All other parameters are as in Fig. 2(c).

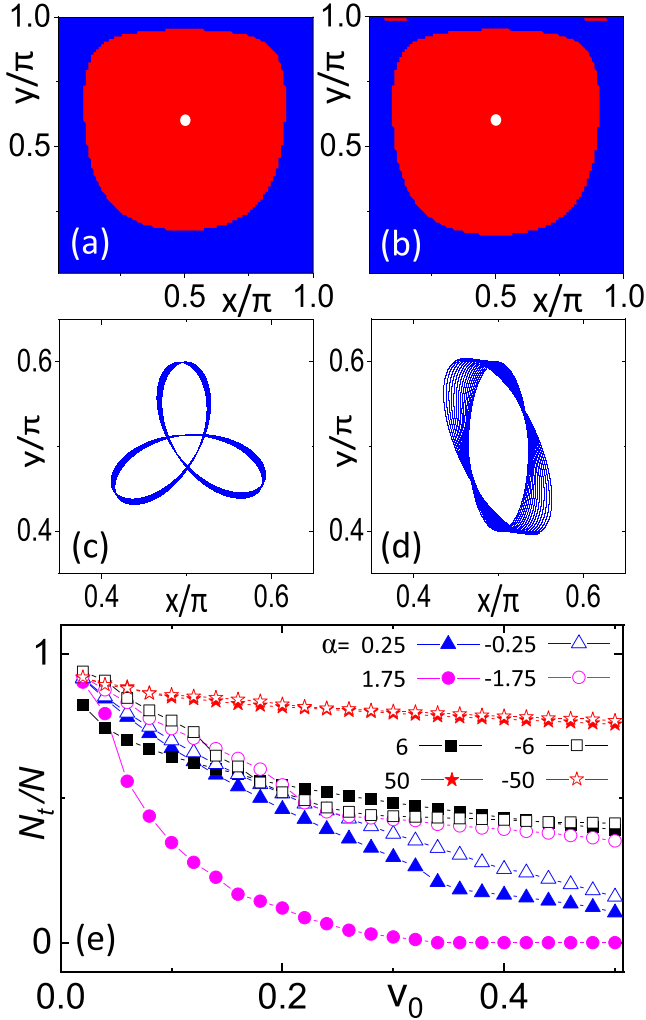


FIG. 10. Trapping regions for negative advection torque,  $\alpha = -0.5$  (a),(c) and  $\alpha = -1$  (b),(d). The initial conditions of the trajectories of length  $t = 10^2$  in (c) and (d) are  $(x(0), y(0), \theta(0)) = (0.5, 0.6, 0)\pi$ ; all other parameters are as in Fig. 2(c). The white dots in (a) and (b) denote the starting point at  $t = 0$ . (e) Fraction of trapped trajectories,  $N_t/N$  vs  $v_0$ , for different positive and negative  $\alpha$  (see legend) to be compared with Fig. 3(d).

Lagrangian chaos may explain the convergence issues encountered in the numerical analysis of the diffusive properties of a noisy active particle in the advection field of Eq. (1) [14]. For instance, in the limit of vanishing translational noise,  $D_0 = 0$  (and zero angular noise), the spatial diffusion at low self-propulsion speeds is certainly dominated by Lagrangian

chaos, which, as shown here, may require exceedingly long simulation runs to be established.

#### ACKNOWLEDGMENTS

Y.L. is supported by the National Natural Science Foundation of China under Grants No. 12375037 and No. 11935010. F.M. and Y.L. are supported by the National Natural Science Foundation of China under Grant No. 12350710786.

#### APPENDIX

As mentioned in Sec. II, at fixed  $v_0$  the trapping regions for  $\alpha = 1$  are smaller than for  $\alpha = 0$  [6,7]. This is a chirality effect induced by the advection torque of strength  $\alpha$  introduced in the third of the Eqs. (3).

To illustrate this point, in Figs. 8 and 9 we characterized the particle's dynamics following the approach as in Sec. II, but for a tunable  $\alpha$ . The area of the trapping regions shrinks with increasing  $\alpha$ , and for  $\alpha > 1$  they reveal a more complex topology. This effect, clearly due to the nonlinearity of Eqs. (3), rests outside the purpose of the present study.

To fully explore the parameter space of our model, in Fig. 10 we also considered the case of negative  $\alpha$  values: for increasingly negative  $\alpha$  values, the trapping regions expand, while the particles injected there keep tracing bounded (but, in general, not closed) orbits around the center of the convection roll.

The different particle's dynamics for positive and negative  $\alpha$  can be qualitatively explained observing that for  $\alpha > 0$  the circulation in the roll and the self-propulsion vector rotation are parallel (i.e., both oriented counterclockwise). This enhances the centripetal push on the particle, thus making its orbit expand for  $0 < \alpha < \Omega_L$ , as displayed in Fig. 9. [Note that, on further increasing  $\alpha$  above  $\Omega_L$ , the advection torque wins over the roll circulation and the orbits tend to shrink (not shown).] Vice versa, in Fig. 10, for  $\alpha < 0$  the circulation and torque due to advection are opposite, so that the particle orbits tend to slowly shrink with increasing the modulus of  $\alpha$ . As a consequence, the area of the trapping regions decrease (increase) with increasing  $|\alpha|$  for positive (negative) values. This occurrence is confirmed by the  $\alpha$  dependence of the curves  $N_t/N$  vs  $v_0$ , displayed in Fig. 10(e).

Notice that for the sake of a purely mathematical analysis, in this Appendix we have treated the strength of the advection torque as a free parameter, whereas, according to Faxén theory [27],  $\alpha$  is determined by the geometry and the chemical-physical properties of the particle surface.

[1] S. Chandrasekhar, *Hydrodynamic and Hydromagnetic Stability* (Oxford University Press, New York, 1967).  
 [2] P. Tabeling, Two-dimensional turbulence: A physicist approach, *Phys. Rep.* **362**, 1 (2002).  
 [3] N. Khurana, J. Blawdziewicz, and N. T. Ouellette, Reduced transport of swimming particles in chaotic flow due to hydrodynamic trapping, *Phys. Rev. Lett.* **106**, 198104 (2011).

[4] G. B. Jeffery, The motion of ellipsoidal particles immersed in a viscous fluid, *Proc. R. Soc. Lond. A* **102**, 161 (1922).  
 [5] A. Zöttl and H. Stark, Nonlinear dynamics of a microswimmer in Poiseuille flow, *Phys. Rev. Lett.* **108**, 218104 (2012).  
 [6] H. Stommel, Trajectories of small bodies sinking slowly through convection cells, *J. Mar. Res.* **8**, 24 (1949).

- [7] M. R. Maxey and S. Corrsin, Gravitational settling of aerosol particles in randomly oriented cellular flow fields, *J. Atmos. Sci.* **43**, 1112 (1986).
- [8] L. P. Wang, M. R. Maxey, T. D. Burton, and D. E. Stock, Chaotic dynamics of particle dispersion in fluids, *Phys. Fluids A* **4**, 1789 (1992).
- [9] A. Sarracino, F. Cecconi, A. Puglisi, and A. Vulpiani, Nonlinear response of inertial tracers in steady laminar flows: Differential and absolute negative mobility, *Phys. Rev. Lett.* **117**, 174501 (2016).
- [10] M. N. Rosenbluth, H. L. Berk, I. Doxas, and W. Horton, Effective diffusion in laminar convective flows, *Phys. Fluids*, **30**, 2636 (1987).
- [11] B. I. Shraiman, Diffusive transport in a Rayleigh-Bénard convection cell, *Phys. Rev. A* **36**, 261 (1987).
- [12] A. M. Soward, Fast dynamo action in a steady flow, *J. Fluid Mech.* **180**, 267 (1987).
- [13] W. Young, A. Pumir, and Y. Pomeau, Anomalous diffusion of tracer in convection rolls, *Phys. Fluids A* **1**, 462 (1989).
- [14] Y. Li, L. Li, F. Marchesoni, D. Debnath, and P. K. Ghosh, Diffusion of chiral Janus particles in convection rolls, *Phys. Rev. Res.* **2**, 013250 (2020).
- [15] C. Torney and Z. Neufeld, Transport and aggregation of self-propelled particles in fluid flows, *Phys. Rev. Lett.* **99**, 078101 (2007).
- [16] S. Jiang and S. Granick (Eds.), *Janus Particle Synthesis, Self-Assembly and Applications* (RSC Publishing, Cambridge, 2012).
- [17] A. Walther and A. H. E. Müller, Janus particles: Synthesis, self-assembly, physical properties, and applications, *Chem. Rev.* **113**, 5194 (2013).
- [18] M. C. Marchetti, J. F. Joanny, S. Ramaswamy, T. B. Liverpool, J. Prost, M. Rao, and R. A. Simha, Hydrodynamics of soft active matter, *Rev. Mod. Phys.* **85**, 1143 (2013).
- [19] J. Elgeti, R. G. Winkler, and G. Gompper, Physics of microswimmers, single particle motion and collective behavior: A review, *Rep. Prog. Phys.* **78**, 056601 (2015).
- [20] Y.-N. Young and M. J. Shelley, Stretch-coil transition and transport of fibers in cellular flows, *Phys. Rev. Lett.* **99**, 058303 (2007).
- [21] S.-Y. Hu, J.-J. Chu, M. J. Shelley, and J. Zhang, Lévy walks and path chaos in the dispersal of elongated structures moving across cellular vortical flows, *Phys. Rev. Lett.* **127**, 074503 (2021).
- [22] P. E. Kloeden and E. Platen, *Numerical Solution of Stochastic Differential Equations* (Springer, Berlin, Heidelberg, 1992).
- [23] Q. Yin, Y. Li, F. Marchesoni, T. Debnath, and P. K. Ghosh, Exit times of a Brownian particle out of a convection roll, *Phys. Fluids* **32**, 092010 (2020).
- [24] C. Gardiner, *Stochastic Methods: A Handbook for the Natural and Social Sciences* (Springer, Berlin, 2009).
- [25] J. M. Sancho, A. M. Lacasta, K. Lindenberg, I. M. Sokolov, and A. H. Romero, Diffusion on a solid surface: Anomalous is normal, *Phys. Rev. Lett.* **92**, 250601 (2004).
- [26] A. Crisanti, M. Falcioni, A. Vulpiani, and G. Paladin, Lagrangian chaos: Transport, mixing and diffusion in fluids, *Riv. Nuovo Cim.* **14**, 1 (1991).
- [27] J. K. G. Dhont, *An Introduction to Dynamics of Colloids* (Elsevier, Amsterdam, 1996).